Computers and Fluids xxx (xxxx) xxx

Contents lists available at ScienceDirect

Computers and Fluids

journal homepage: www.elsevier.com/locate/compfluid

Numerical study of rising bubbles with path instability using conservative level-set and adaptive mesh refinement

Oscar Antepara[a,b,*], Néstor Balcázar[b], Joaquim Rigola[a], Assensi Oliva[a,*]

[a] Heat and Mass Transfer Technological Center (CTTC), Universitat Politècnica de Catalunya - BarcelonaTech (UPC) ESEIAAT, Colom 11, Terrassa 08222, Barcelona, Spain
[b] Termo Fluids, S.L., Avda Jacquard 97 1-E, Terrassa 08222, Barcelona, Spain

ARTICLE INFO

Article history:
Received 11 September 2018
Revised 12 April 2019
Accepted 20 April 2019
Available online xxx

Keywords:
Wobbling bubble
Path instability
Direct numerical simulation
Conservative level-set
Adaptive mesh refinement

ABSTRACT

This paper focuses on three-dimensional direct numerical simulations of rising bubbles in the wobbling regime, and the study of its dynamical behavior for Eötvös number $1 \leq Eo \leq 10$ and Morton number $1e{-}11 \leq M \leq 1e{-}9$. The computational methodology is based on a mass Conservative Level-Set method, whereas the spatial discretization of the computational domain employs an Adaptive Mesh Refinement strategy for the reduction of computational resources. The Navier–Stokes equations are discretized using the finite-volume approach on a collocated unstructured mesh; the pressure-velocity coupling is solved using a classical fractional-step projection method. This methodology is applied to a series of verification and validation tests, which are compared with experiments and numerical results from the literature. Finally, buoyancy bubbles rising in the wobbling regime are researched at moderate to high Reynolds numbers ($100 < Re < 3000$). Terminal Reynolds number, drag coefficient and frequency of path oscillations are compared with empirical correlations and numerical studies from the literature. Results show the discharge of alternate oppositely-oriented hairpin vortex structures. Moreover, depending on the characteristics numbers of the system, different path features, bubble shape, and vortical structures in the wake are reported.

1. Introduction

The phenomenon of a bubble rising in a quiescent liquid due to gravity has been studied over the last decades. Many experimental studies have demonstrated that gas bubbles rising in liquids stop following a straight vertical line, and start to ascend in different path motions Duineveld [23], Prosperetti [49], Prosperetti et al. [50], Saffman [52]. As a result, this phenomenon, in which the effects of gravity, surface tension, and liquid inertia are intimately coupled, has motivated numerous investigations. However, there are still open questions about the intrinsic mechanism that leads to a wake disruption, bubble deformations, periodic variations of the velocity, and different path motions. Therefore, the main motivation of this research is to contribute to the understanding of these phenomena.

Direct numerical simulation (DNS) of multiphase systems has become an important research tool for the study of bubbles and droplets, where the interface capturing is a relevant issue. Concerning the interface capturing, several methods can be employed, i.e. Front Tracking (FT) method Tryggvason et al. [66], Unverdi and Tryggvason [67], Level Set (LS) method Balcázar et al. [3], Olsson and Kreiss [44], Osher and Sethian [45], Sussman et al. [57]) and the Volume Of Fluid (VOF) method (Hirt and Nichols [34], Van Sint Annaland et al. [68]. In FT methods [66,67], the interface is located in a Lagrangian way across a stationary Eulerian grid. This method is accurate but rather complex to implement when topology changes. The VOF methods [34,68] use a color function to identify the interface, corresponding to the volume fraction within each cell of one of the fluids.

As a consequence, the VOF function needs to be advected and reconstructed by geometric techniques. Its main advantage is to accurately advect the interface, keeping a sharp interface to conserve the mass. However, it presents difficulties to compute accurate curvatures from the color function, because of its step discontinuity. In LS methods [45,57], the interface is defined as a zero-contour of a smooth signed distance function. With this approach, interface curvatures and normals can be accurately evaluated, although mass is not always conserved. Mass conservation issue can be circumvented in the context of Conservative Level-Set (CLS) methods [44], where a regularized indicator function is used in place of the

* Corresponding author.
E-mail addresses: oscar@cttc.upc.edu, oscarantepara@gmail.com (O. Antepara), cttc@cttc.upc.edu (A. Oliva).

https://doi.org/10.1016/j.compfluid.2019.04.013
0045-7930/

signed distance function. Recently, a finite-volume CLS method has been introduced by Balcázar et al. [3] for two-phase flows with surface tension on unstructured grids. Further advantages of the CLS method include an accurate computation of surface tension, numerical stability, and efficient parallelization as demonstrated in our previous works [3–5,7,8].

Regarding experimental research for the wobbling regime, unstable bubble wake and paths have been researched by De Vries et al. [21], Ern et al. [25], Magnaudet and Eames [39], Magnaudet and Mougin [40], Tchoufag et al. [60]. Saffman [52] has reported zigzagging and spiraling bubbles, whose trajectory highly depends on bubble size and complex physical mechanisms. Ellingsen and Risso [24] described path motions in the absence of shape oscillations. Lunde and Perkins [38] have shown a relation between the zigzagging path and the periodic shedding of vortices. Moreover, Brücker [12], Veldhuis et al. [69] pointed out a description of shape oscillations and the formation of vortical hairpin structures attached to the lower side of the rising bubble in a zigzagging and spiral path. Although previous investigators have made a significant contribution, detailed studies of the evolution of the flow, exact experimental conditions, and a full description of the interface are not precisely determined.

The continued lack of understanding of this phenomenon has motivated numerical research of buoyancy rising motion of gas bubbles in a stagnant liquid (Balcázar et al. [5], Esmaeeli et al. [26], Hua et al. [35], Smolianski et al. [56]). Mougin and Magnaudet [41], [42] model the problem considering the bubble as a fixed shape, coupling Navier–Stokes equations with force and torque balances. Cano-Lozano et al. [16], [17], Sharaf et al. [55], Tripathi et al. [65] reported simulations with frozen bubble shapes and deformable nearly spheroidal bubbles, using the VOF method and fixed grid approach. Albert et al. [1], Bothe [13], Bothe et al. [14], Koebe et al. [37] studied the rise dynamics of various cases of bubbles and droplets, where various tests with different bubble/droplets sizes and dimensionless numbers were reported. Baltussen et al. [9] presented a comparison between various VOF models and compared the terminal Reynolds with experimental correlations for cases in the wobbling regime. Pivello et al. [47] introduced a methodology using Front Tracking and adaptive mesh refinement(AMR) for simulating wobbling bubbles. Gaudlitz and Adams [29] used a Particle Level Set in a periodic domain showing the wake and shape variations of an air bubble rising in water.

Most of the previous numerical studies agree on the challenge of the DNS for the rising bubbles in the wobbling regime, and the difficulties in capturing the phenomena for medium to high Reynolds numbers. Furthermore, some challenges arise for the need for larger grids, improved models for capturing phase interfaces, and enough grid resolution for capturing the wake and the vortical structures present in this phenomenon.

In this context, and to the best of authors' knowledge, there are no previous studies of buoyancy-driven rising bubbles at high Reynolds numbers, i.e., Re O(1000), by using a conservative level-set method and adaptive mesh refinement. Therefore, the objectives of this contribution are twofold: the first goal is to present an improved numerical methodology for simulating rising bubbles with path instabilities, based on the conservative level-set method (Balcázar et al. [3], [7]) for interface capturing on general meshes, integrated to an adaptive mesh refinement framework (Antepara et al. [2]) for optimization of computational resources in large spatial domains. The second goal is to perform numerical research of the effect of Eötvös number and Morton number on the motion of rising bubbles with path instability, by using the improved framework. As aforementioned, the present research is based on an unstructured finite-volume/CLS method introduced in [3,7]. As a consequence, the mass conservation issue inherent to standard level-set methods is circumvented, whereas the grid can be adapted to complex domains, enabling for an efficient mesh distribution in regions where interface resolution has to be maximized, by using an adaptive mesh refinement strategy introduced in [2]. Furthermore, unstructured flux-limiter schemes introduced in [3] are used to advect the CLS function in interface propagation equation, as well as the velocity in momentum equation, to avoid numerical oscillations around discontinuities, whereas the numerical diffusion is minimized. Finally, the present finite-volume formulation [3] is attractive due to its simplicity and the satisfaction of the integral forms of the conservation laws over the entire domain.

The outline of the paper is as follows: A summary of the governing equations and numerical methods are given in Section 2. The coupling of the Navier-Stokes equations for two-phase flow and the description of the CLS method are introduced. Moreover, a description of the AMR implementation is shown. The code validation and numerical results for wobbling bubbles are displayed in Section 3. The conclusions are presented in Section 4.

2. Mathematical model and numerical methods

2.1. Incompressible two-phase flow

Two immiscible incompressible and Newtonian fluids are described by the Navier–Stokes equations defined by a single fluid in the domain Ω, with a singular source term for the surface tension force at the interface Γ (see [3,11,15,46]):

$$\frac{\partial}{\partial t}(\rho\mathbf{v}) + \nabla\cdot(\rho\mathbf{v}\mathbf{v}) = -\nabla p + \nabla\cdot\mu\left[\nabla\mathbf{v} + (\nabla\mathbf{v})^T\right] + \rho\mathbf{g} + \sigma\kappa\mathbf{n}\delta_\Gamma, \tag{1}$$

$$\nabla\cdot\mathbf{v} = 0, \tag{2}$$

where ρ and μ are the density and dynamic viscosity of the fluids, $\mathbf{g}$ is the gravity acceleration, p is the pressure, $\mathbf{v}$ is the velocity field, the super-index T represents the transpose operator, δ_Γ is a Dirac delta function at the interface Γ, σ is the surface tension coefficient, κ is the curvature of the interface, and $\mathbf{n}$ denotes the normal unit vector on the interface. Physical parameters change discontinuously across the interface:

$$\begin{aligned}\rho &= \rho_1 H_1 + \rho_2(1-H_1) \\ \mu &= \mu_1 H_1 + \mu_2(1-H_1),\end{aligned} \tag{3}$$

with ρ_1, ρ_2 and μ_1, μ_2 being the densities and viscosities of the first and second fluids, respectively. Whereas, H_1 is the Heaviside step function that is one at fluid 1, and zero elsewhere. At the discretized level, physical properties are smoothed according to the CLS method (see [3]).

2.2. Conservative level set equations

The conservative level-set method as introduced in [3] for interface capturing on unstructured meshes is used in this work. While the standard level-set method [57] uses a signed distance function d(x, t) to represent the interface, the CLS method employs a regularized indicator function, ϕ, as follows:

$$\phi(\mathbf{x},t) = \frac{1}{2}\left\{tanh\left[\frac{d(\mathbf{x},t)}{2\varepsilon}\right] + 1\right\}, \tag{4}$$

where $\varepsilon = 0.5h^{0.9}$ is a tunable parameter which sets the thickness of the profile, and h is the grid size. With this profile the interface Γ is defined by the location of the iso-surface $\phi = 0.5$:

$$\Gamma = \{\mathbf{x} \mid \phi(\mathbf{x},t) = 0.5\}. \tag{5}$$

Please cite this article as: O. Antepara, N. Balcázar and J. Rigola et al., Numerical study of rising bubbles with path instability using conservative level-set and adaptive mesh refinement, Computers and Fluids, https://doi.org/10.1016/j.compfluid.2019.04.013

Since the level-set function is advected by the fluid velocity field, the following interface transport equation can be derived:

$$\frac{\partial \phi}{\partial t} + \nabla \cdot \phi \mathbf{v} = 0. \tag{6}$$

The level-set function must be reinitialized to keep the profile and thickness of the interface constant, following the next equation:

$$\frac{\partial \phi}{\partial \tau} + \nabla \cdot \phi(1-\phi)\mathbf{n} = \nabla \cdot \varepsilon \nabla \phi. \tag{7}$$

This equation advances in pseudo-time τ, and consists of a compressive term, $\nabla \cdot \phi(1-\phi)\mathbf{n}$, which compress the level-set function onto the interface along the normal vector $\mathbf{n}$, and of a diffusion term $\nabla \cdot \varepsilon \nabla \phi$ which keeps the profile with a characteristic thickness ε.

The reader is referred to [3,7] for further details on the implementation of the conservative level-set method used in this work.

2.3. Surface tension and regularization of fluid properties

Implementing surface tension in a numerical method involves two issues: the curvature κ needs to be determined and the pressure jump should be applied appropriately to the fluids. These problems are addressed in the context of the continuous surface force model (CSF) introduced by [11]. Thus, the term, $\sigma \kappa \mathbf{n} \delta_\Gamma$, is converted to a volume force as follows:

$$\sigma \kappa \mathbf{n} \delta_\Gamma = \sigma \kappa(\phi) \nabla \phi, \tag{8}$$

where $\kappa(\phi)$ and $\mathbf{n}$ are given by

$$\mathbf{n} = \frac{\nabla \phi}{||\nabla \phi||}, \tag{9}$$

$$\kappa(\phi) = -\nabla \cdot \mathbf{n}. \tag{10}$$

Following the work of [3], $\nabla \phi$ is computed using the least-squares method with the information of the neighbor cells around the vertices of the current cell. In addition, the fluid properties are regularized using the level-set function. Therefore, the density and viscosity fields are calculated as follows:

$$\begin{aligned} \rho &= \rho_1 \phi + \rho_2 (1-\phi) \\ \mu &= \mu_1 \phi + \mu_2 (1-\phi). \end{aligned} \tag{11}$$

2.4. Numerical methods

The governing equations have been discretized using a finite-volume(FV) approach on a collocated unstructured grid arrangement according to [3], which automatically adapts to the AMR framework. Convective terms are discretized using a Total Variation Diminishing (TVD) Superbee flux limiter scheme (see [3]), to avoid numerical oscillations at the discontinuities, and minimize numerical diffusion (comparison between different convective schemes in rising bubble cases is presented in Section 3.1.3). Diffusive terms are discretized employing a central difference scheme. Gradients are computed at cell centroids using the least-squares method, and a distance-weighted linear interpolation is used to calculate the values of physical properties, gradients and interface normals at the cell faces (see [3]), unless otherwise stated. A central difference scheme is employed to discretize both compressive and diffusive terms of the re-initialization Eq. (7). A standard fractional step projection method is used for solving the pressure-velocity coupling (see [7,19]):

$$\frac{\rho \mathbf{v}^* - \rho^n \mathbf{v}^n}{\Delta t} = \mathbf{A}^n + \mathbf{D}^n + \rho \mathbf{g} + \sigma \kappa \nabla_h(\phi), \tag{12}$$

$$\mathbf{v} = \mathbf{v}^* - \frac{\Delta t}{\rho} \nabla_h(p), \tag{13}$$

where super-index n denotes the previous time step, $\mathbf{A} = -\nabla_h \cdot (\rho \mathbf{v}\mathbf{v})$, and $\mathbf{D} = \nabla_h \cdot (\mu((\nabla_h \mathbf{v}) + (\nabla_h \mathbf{v})^T))$ are explicitly evaluated, $(\nabla_h \mathbf{v})^T$ is calculated by a vertex-node based least-squares method (see [3]). Combining the incompressible constraint with Eq. (13), a Poisson equation for the pressure field is obtained, which is solved by means of a preconditioned conjugated gradient method:

$$\nabla_h \cdot \left[\frac{1}{\rho} \nabla_h(p) \right] = \frac{1}{\Delta t} \nabla_h \cdot (\mathbf{v}^*), \qquad \mathbf{e}_{\partial\Omega} \cdot \nabla_h p|_{\partial\Omega} = 0. \tag{14}$$

In order to fulfill the incompressible constraint (Eq. (2)), and to avoid pressure-velocity decoupling when the pressure projection is made on collocated meshes (see [51]), a cell face velocity $\mathbf{v}_f$ is defined at each control volume. Namely in discretized form:

$$\mathbf{v}_f = \sum_{q \in \{P,F\}} \frac{1}{2} \left[\mathbf{v}_q + \frac{\Delta t}{\rho(\phi_q)} (\nabla_h p)_q \right] - \frac{\Delta t}{\rho_f} (\nabla_h p)_f, \tag{15}$$

where P and F are denoting the adjacent cell nodes to the face f. The reader is referred to Appendix B of our previous work (see.[7]) for additional technical details on the origin of Eq. (15). The time increment Δt, which is limited by the CFL conditions and the stability condition for the capillary force (see [11]), is given by:

$$\Delta t = C_{\Delta t} min \left[\frac{h}{||\mathbf{v}||}, \frac{\rho h^2}{\mu}, \left(\frac{h}{||\mathbf{g}||} \right)^{1/2}, h^{3/2} \left(\frac{\rho_1 + \rho_2}{4\pi\sigma} \right)^{1/2} \right], \tag{16}$$

where $C_{\Delta t} = 0.1$ for the current method and $h = (V_p)^{1/3}$ is defined as the characteristic size of the control volume P. Finally, a TVD Runge–Kutta method [31] is used for time integration of advection Eq. (6) and re-initialization Eq. (7). The time step for re-initialization Eq. (7) is restricted by its viscous term as follows $\Delta \tau = C_\tau min((h^2)/\varepsilon)$, where C_τ is taken to be ~ 0.05. For the present simulations, one re-initialization step is enough to achieve the steady state of Eq. (7).

The numerical algorithms explained in this work are implemented in a parallel C++/MPI code called TermoFluids (see as an example [3,27,61,64]). The code has been executed on the supercomputer MareNostrum IV using up to 144 cores for 3D simulations of wobbling bubbles. Furthermore, the numerical methods used in this work have been extensively validated with experiments and numerical results from the literature, including 2D dam-break [3], 2D and 3D rising bubbles [3,5,6], bubbly flows [4,8], droplet deformation in a shear flow [6], droplet collision against a fluid-fluid interface and binary droplet collision with bouncing outcome [4], thermocapillary-driven motion of deformable fluid particles [7], Taylor bubbles [33], and atomization of a liquid-gas jet [53,54]. Therefore, this research can be considered as a further step in the understanding of the physics of rising bubbles with path instability at high Reynolds numbers, with the aid of a CLS method introduced by [3] and adaptive mesh refinement method given by [2].

2.5. Adaptive mesh refinement

The use of Adaptive Mesh Refinement algorithms for the solution of multiphase problems has been presented by various authors [18,35,47,48,58], which is becoming an effective tool for demanding computational problems.

In this work, the Conservative Level Set method (see [3]) for tracking the interface in a continuous medium and adaptive mesh refinement to ensure a good mesh resolution in the interface profile and in the near wake where the vortices appear for most of the rising bubble problems are used. The adaptive mesh refinement employs an octree decomposition to be able to do the refinement and coarsening process in a proper way, and a 1:2 re-

Please cite this article as: O. Antepara, N. Balcázar and J. Rigola et al., Numerical study of rising bubbles with path instability using conservative level-set and adaptive mesh refinement, Computers and Fluids, https://doi.org/10.1016/j.compfluid.2019.04.013

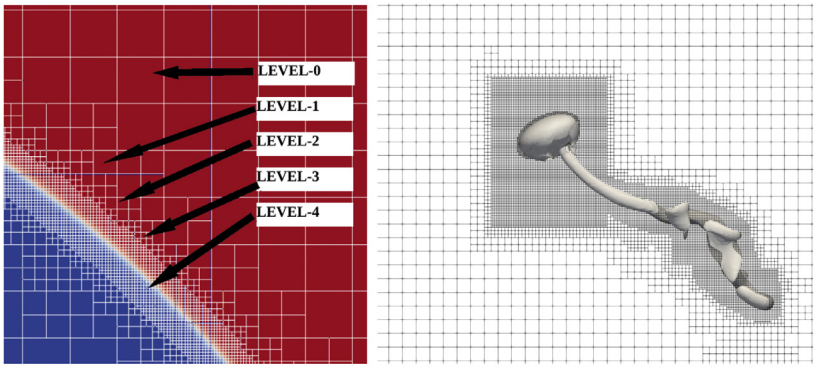

Fig. 1. Illustration of the refinement procedure for (a) level-set function ϕ, where four levels of refinement have been applied; (b) 3D box and the vorticity function.

lation between the different refinement levels is kept (see Fig. 1). The reader is referred to as [2] for further details on the adaptive mesh refinement algorithm applied to this paper. Furthermore, our hexahedral AMR algorithm has been validated with numerical results from the literature, including LES of turbulent flows around bluff bodies [2], atomization of a liquid-gas jet [53,54], and as local mesh refinement for conjugate heat transfer problems [28].

The AMR is included in the global algorithm developed for the CLS method (see [3]), and the AMR loop is reinitialized when the centroid of the bubble has moved a distance equal to the minimum grid size in the computational domain Ω. The global algorithm for the coupled AMR-CLS consists of the following steps:

1. Calculate the minimum grid size $h_{\min}$ in Ω.
2. Calculate the initial position of the bubble centroid b_{co}.
3. Calculate Δt by Eq. (16).
4. Solve level-set advection Eq. (6).
5. Solve re-initialization Eq. (7) for steady state.
6. Physical properties (ρ, μ) are updated according to Section 2.3
7. Calculate $\mathbf{v}$ and p by the fractional-step method:
   (a) Calculate the predicted velocity by Eq. (12).
   (b) Solve Eq. (14) for pressure.
   (c) Calculate the corrected velocity by Eq. (13).
8. Calculate $\mathbf{v}_f$ by Eq. (15).
9. Calculate the actual position of the bubble centroid b_c.
10. **if** ($||b_c - b_{co}|| < h_{\min}$) Repeat steps 3–8.
    else Re-mesh and repeat steps 1–8 until the desired time-level is reached.

The Re-mesh step from the CLS-AMR algorithm follows the following criteria for the rising bubbles in quiescent liquid:

1.- Interface capturing function. The level-set function ϕ is used to identify the interface between fluids, and locally refine the mesh when $0 + \epsilon < \phi < 1 - \epsilon$, where $\epsilon = 1e-4$. Moreover, to avoid the refinement process to be often repeated, up to three layers of neighboring cells adjunct to the interface profile will also be refined. This is done to give enough spatial displacement for the interface to move in any direction ensuring a good mesh resolution. Fig. 1 is an example of a level-set function and its neighboring cells with a grid spacing of four levels of refinement.

2.- 3D Box. The near wake of the bubble is essential for the correct development of the vortical structures which will appear at the lower side of the rising bubbles. Therefore, a box around the bubble will be refined depending on the bubble diameter. This procedure is described in the numerical experiments section.

3.- Vorticity function. This function is used to capture the vortical structures that appear in the near wake of the rising bubble. The vorticity field is calculated following the next equation,

$$\omega = \nabla \times \mathbf{v}. \tag{17}$$

The vorticity values which are positive identify clockwise rotating vortices, and the negative values are related to anti-clockwise rotation. With the vorticity magnitude field $||\omega||$, the cells to be refined as the ones with vorticity values over the 10% of the maximum value for the entire field were established, to capture the primary vortical structures. Furthermore, three layers of neighbors cells are also refined to ensure enough grid resolution for the vortical structures.

3. Numerical experiments

In this section, numerical tests for verification and validation are described, and new numerical experiments related to wobbling bubbles will be analyzed. According to [10,20], the dimensionless numbers controlling the rising bubble in a quiescent liquid are the Eötvös number (Eo), Reynolds number (Re), Morton number (M) and the ratios of physical properties (density ratio η_ρ and viscosity ratio η_μ), defined as follows

$$Eo = \frac{gd^2\Delta\rho}{\sigma}, \quad M = \frac{g\mu_1^4\Delta\rho}{\rho_1^2\sigma^3}, \quad Re = \frac{\rho_1 U_T d}{\mu_1}, \quad \eta_\rho = \frac{\rho_1}{\rho_2}, \quad \eta_\mu = \frac{\mu_1}{\mu_2}, \tag{18}$$

where the subindex 1 refers to the continuous fluid phase, the subindex 2 refers to the lighter fluid in the bubble, d refers to the bubble diameter and $\Delta\rho = \rho_1 - \rho_2$ specifies the density difference between the fluid phases. The terminal velocity of the bubble is defined by,

$$U_T = \frac{\int_{\Omega_2} v_y \phi dV}{\int_{\Omega_2} dV}, \tag{19}$$

and we also introduce the following dimensionless time, $t^* = t\sqrt{g/d}$. Furthermore, in order to get a quantitative measure of the bubble shape, the sphericity is defined as

$$\zeta = \frac{\pi d^2}{\int_\Omega ||\nabla\phi|| dV}. \tag{20}$$

3.1. Verification and validation

A selection of numerical tests, with an increase of the grid resolution, are presented to show the accuracy of the numerical method. For the stationary drop test, the starting grid size consists of 20 control volume per diameter and is increased up to 80 control volumes per diameter. For the experimental validation and the

Please cite this article as: O. Antepara, N. Balcázar and J. Rigola et al., Numerical study of rising bubbles with path instability using conservative level-set and adaptive mesh refinement, Computers and Fluids, https://doi.org/10.1016/j.compfluid.2019.04.013

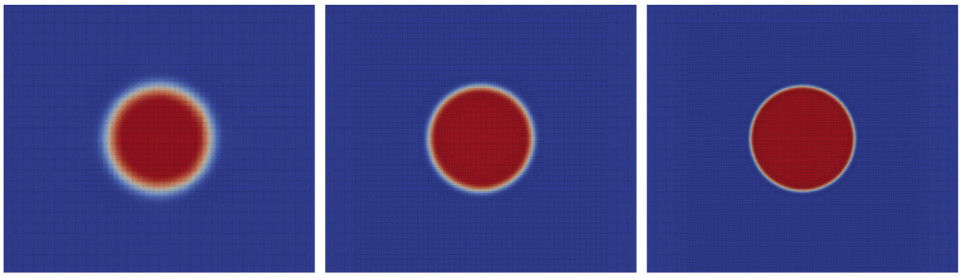

Fig. 2. Mid-section plane for the 3D static drop test with different grid resolutions using AMR, where the pressure distribution is shown. (a) $d/20$, (b) $d/40$, (c) $d/80$.

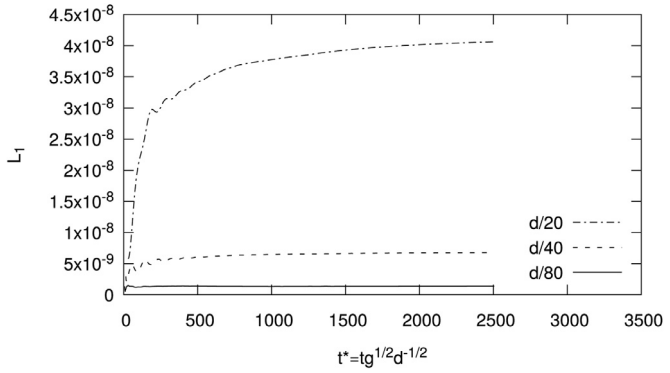

Fig. 3. Time evolution of the error for the dimensionless velocity, Eq. (23), on different grid resolutions.

wobbling bubbles, the starting grid size consists of 15 control volumes per diameter and is increased up to 60 control volumes per diameter, which is a sufficient resolution for simulations covered in this work.

3.1.1. Stationary drop test

This numerical test consists in the solution of a spherical drop, with a diameter d, positioned in the center of a cubic domain with a length of $10d$, without the influence of gravity. The densities are equal to 10^4, the viscosities and the surface tension equal to 1. This test has also been used by [6,36] for unstructured meshes. A steady solution is originated where the pressure jump can be calculated and compared to an analytical solution provided by the Laplace equation,

$$\Delta P_{exact} = \sigma \kappa_{exact}, \tag{21}$$

where the exact curvature is given by $\kappa_{exact} = 4/d$ for a spherical drop. The exact solution is a zero velocity field, and the pressure jump at the droplet interface is given by $\Delta P = \frac{4\sigma}{d}$. Present test cases are solved on a uniform mesh where AMR is applied, as can be seen in Fig. 2.

The error of the pressure jump is calculated by using pressure values inside (p_{in}) and outside (p_{out}) of the drop,

$$E(\Delta P) = \frac{|p_{in} - p_{out} - 4\sigma/d|}{4\sigma/d}. \tag{22}$$

Moreover, spurious currents arise as a consequence of the imbalance between surface tension and the pressure around the drop, which can be measured following the L_1 error norm:

$$L_1(\mathbf{v}) = \frac{1}{N_{cells}} \sum_{k}^{N_{cells}} (\mathbf{v}_k \cdot \mathbf{v}_k)^{1/2} \frac{\mu}{\sigma}, \tag{23}$$

which is computed on the whole spatial domain. In Table 1, the numerical error for the pressure jump and the spurious velocities are shown and compared when the grid resolution is increased.

Table 1
Errors for the dimensionless velocity and pressure for different grid resolution. Here p is the order of convergence.

h	$L_1(\mathbf{v})$	$E(\Delta P)$
1/20	$4.1e-08$	0.020
1/40	$6.8e-09$	0.0029
1/80	$1.4e-09$	0.00041
$p \approx$	2.4	2.8

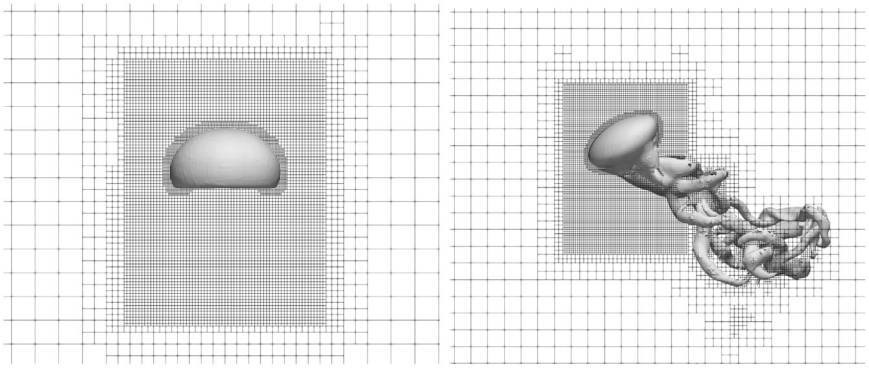

Fig. 4. AMR with an effective grid resolution of 60 control volumes per diameter at the interface, and 30 control volumes per diameter for the vortical structures and the near wake. (a) Eo = 116, M = 41.1, (b) Eo = 3.6, M = 2.5e−11.

Please cite this article as: O. Antepara, N. Balcázar and J. Rigola et al., Numerical study of rising bubbles with path instability using conservative level-set and adaptive mesh refinement, Computers and Fluids, https://doi.org/10.1016/j.compfluid.2019.04.013

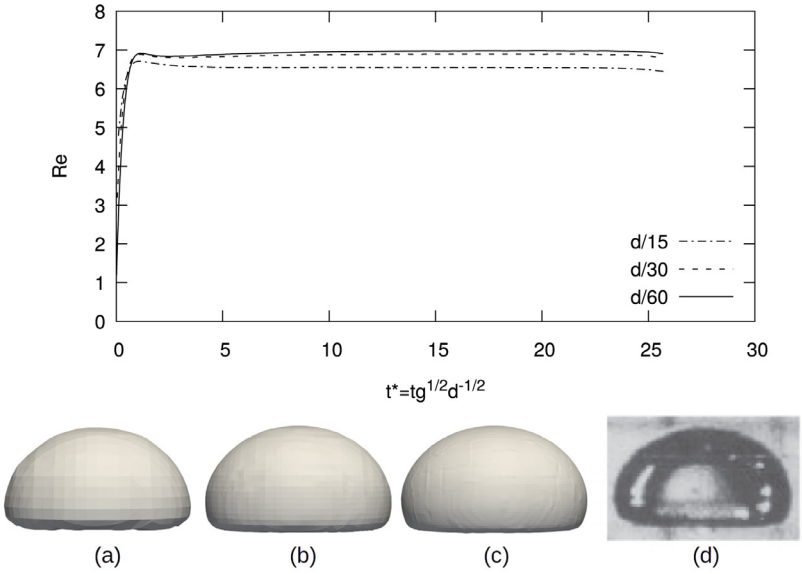

Fig. 5. Grid convergence and final bubble shape for Eo =116, $M = 41.1$. (a) $d/15$, (b) $d/30$, (c) $d/60$, (d) Experiment [10].

The spurious current and pressure jump errors diminish with an order of convergence of second order. Moreover, the spurious current magnitude tends to a steady state as time advances (See Fig. 3). The results above demonstrate the accuracy of the surface tension model.

3.1.2. Grid convergence for ellipsoidal and wobbling bubbles

In this section, the methodology is validated with the rising bubble of ellipsoidal and wobbling bubbles in a quiescent liquid.

The dimensions of the rectangular domain for the ellipsoidal test case are the following: $\Omega = [0, 8d] \times [0, 16d] \times [0, 8d]$, where the initial bubble of diameter $d = 0.25$ is located at $(x, y, z) = (0, d, 0)$. Moreover, the boundary conditions in the top/bottom walls are no-slip, whereas the Neumann condition is applied on the lateral walls and the initial mesh is around 54k control volumes. For the wobbling test case, a vast computational domain is required due to the chaotic and oscillatory path trajectories expected in this regime. The computational domain has a size of $\Omega = [0, 16d] \times [0, 80d] \times [0, 16d]$. The boundary and initial conditions are the same as for the ellipsoidal bubble. The initial mesh is around 1.08 M control volumes.

AMR was used to achieve a desired grid resolution in the interface and the near wake. To assure these conditions a 3D box was refined around the bubble with dimensions of $[2d; 2.75d; 2.0d]$, where the 3D box centroid is relatively located at $(0.0, -0.375d, 0.0)$ with respect to the bubble centroid (See Fig. 4).

Table 2
Present Re computations compared with experimental results by [10], and numerical results by [5,6].

Case Eo =116, $M = 41.1$	Number of control volumes	Re
[10]		7.16
[5]	2.30e+06	6.94
[6]	2.92e+06	7.02
Present AMR-CLS ($d/15$)	8.00e+04	6.55
Present AMR-CLS ($d/30$)	1.64e+05	6.89
Present AMR-CLS ($d/60$)	6.60e+05	6.98

For the ellipsoidal bubble test, the dimensionless numbers are Eo = 116, $M = 41.1$, $\rho_1/\rho_2 = \mu_1/\mu_2 = 100$. In Fig. 5, the terminal Reynolds number for the ellipsoidal test is shown for different grid resolutions. The final bubble shape is consistent with the experimental result of [10], where the bubble reached an ellipsoidal shape with a dimple formation at the rear end.

These results are compared to experiments and numerical solutions from the literature using a fixed mesh (See Table 2). As the resolution increases up to 60 control volumes per bubble diameter, the computed Reynolds number is closer to the experiments reported by [10]. Also, present results are consistent with CLS and VOF/LS simulations reported by [5,6] on fixed meshes.

For the cases of wobbling bubbles, different grid resolutions are compared for Eo = 3.6, $M = 2.5\text{e}{-11}$, $\rho_1/\rho_2 = \mu_1/\mu_2 = 100$. In Fig. 6, Reynolds number, bubble shape and vortical structures

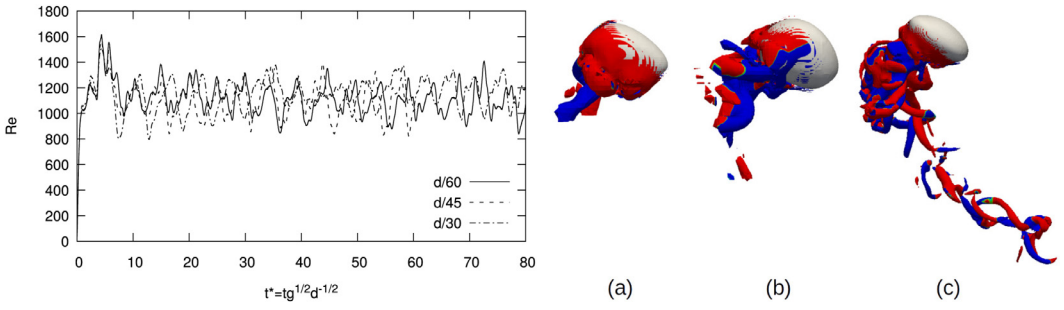

Fig. 6. Reynolds number and bubble shapes at $t^* = 59.5$ for Eo = 3.6, $M = 2.5\text{e}{-11}$. (a) $d/30$, (b) $d/45$, (c) $d/60$.

Please cite this article as: O. Antepara, N. Balcázar and J. Rigola et al., Numerical study of rising bubbles with path instability using conservative level-set and adaptive mesh refinement, Computers and Fluids, https://doi.org/10.1016/j.compfluid.2019.04.013

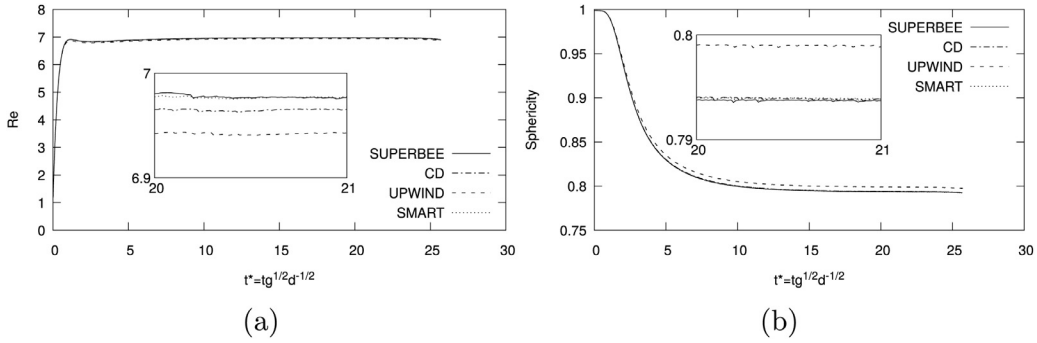

Fig. 7. Effect of the convective scheme used to discretize the momentum Eq. (1) for Eo = 116, M = 41.1 with a grid resolution of d/60 near the interface (a) Re number, (b) Sphericity.

Table 3
Present Re computations compared with experimental result by [32] with different grid resolutions.

Case Eo = 3.6, M = 2.5e−11	Re
[32]	1200
Present AMR-CLS (d/30)	1145.37
Present AMR-CLS (d/45)	1106.36
Present AMR-CLS (d/60)	1105.09

Table 4
Flux limiters $L(\theta)$ used in this work.

	$L(\theta)$
Central difference limiter (CD)	1
TVD Superbee limiter	$max[0, min(2\theta, 1), min(2, \theta)]$
Smart limiter	$max\{0, min[2\theta, (0.25 + 0.75\theta)], 4\}$
First-order upwind limiter	0

are compared with grid resolutions of d/30, d/45 and d/60. As shown, the behavior of the rising velocity becomes chaotic in this regime. Nevertheless, the global qualitative appearance of the terminal Reynolds number (see Fig. 6 and Table 3) are retained as the grid resolution is increased, although the peak velocity at earlier times slightly changes. However, to keep an adequate grid size for the numerical tests presented in this work with mid to high Reynolds number, the resolution of d/60 was chosen for the interface and d/30 for the near wake and vortical structures.

3.1.3. Comparison of different convective schemes and mass conservation for ellipsoidal and wobbling bubbles

Numerical tests have been performed to study the influence of the convective scheme used to discretize momentum Eq. (1), on terminal Reynolds and final shape for ellipsoidal bubbles. Moreover, the effect of the convective schemes in the solution of wobbling bubbles will be discussed. Following the work by [3], the discretization of the convective term of Eq. (1) is based on the use of flux limiters [30,59], $L(\theta)$, defined in the Table 4, where θ is a monitor variable defined as the upwind ratio of consecutive gradi-

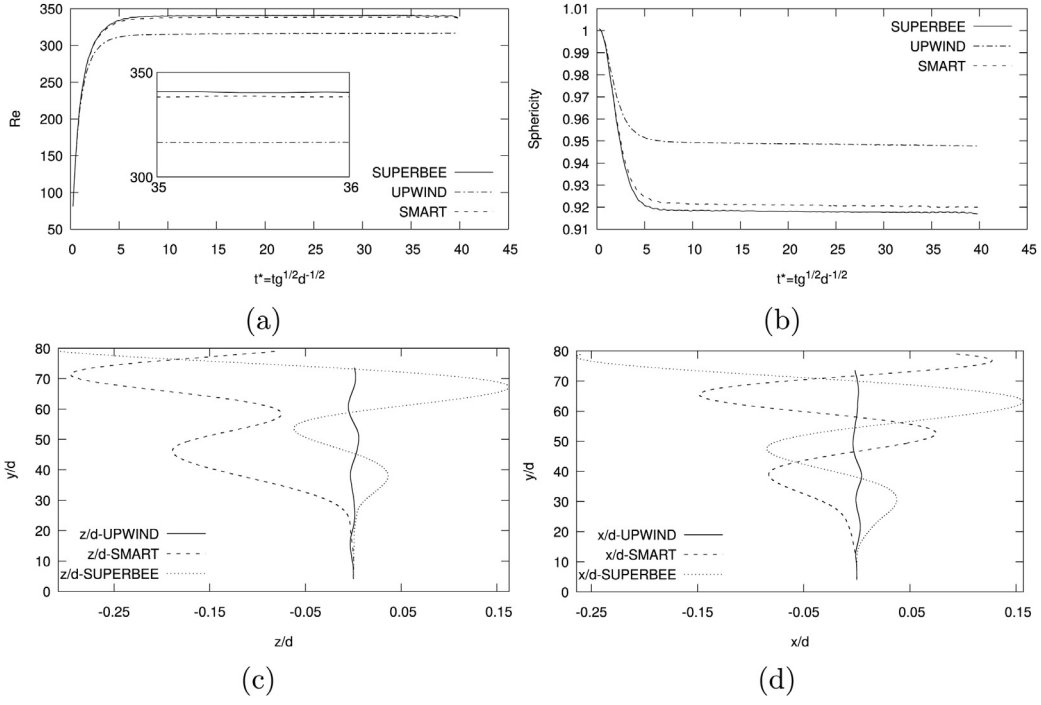

Fig. 8. Effect of the convective scheme for Eo =1, M = 1e−09 with a grid resolution of d/60 near the interface (a) Terminal Re number, (b) Sphericity, (c) Projection of path onto yz-, (d) Projection of path onto yx-.

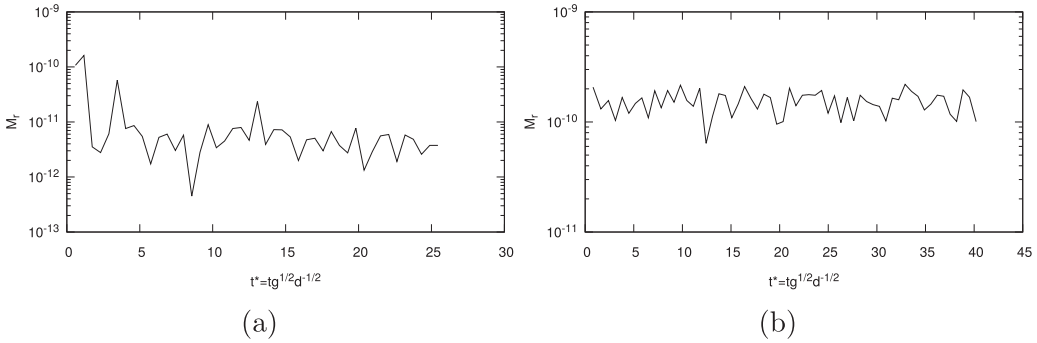

Fig. 9. Mass conservation error for different test cases with a grid resolution of $d/60$ near the interface (a) Eo = 116, M = 41.1 (b) Eo = 1, M = 1e−09.

ents of the velocity components. The reader is referred to [3,5] for technical details on the application of flux limiters to discretize the convective term on unstructured grids.

In Fig. 7, the Central Difference, Upwind, Smart, and Superbee schemes are compared to the solution of terminal Reynolds number and sphericity for the case with Eo = 116, M = 41.1, with the same properties and the finest mesh proposed in Section 3.1.2. As can be seen, the use of different flux limiters leads to similar results for terminal Reynolds number and final bubble shape.

For the cases of wobbling bubbles, the Upwind, Smart, and Superbee schemes are compared for Eo = 1, M = 1e−09. The central difference scheme is out of this review because its behavior was unstable in this regime. In Fig. 8 terminal Reynolds number, sphericity and oscillation paths in different planes are compared. As can be seen, Smart and Superbee perform in the same manner, but the Upwind differs with low amplitude of path oscillation, smaller terminal Reynolds number and less deformation. This behavior can be explained as the Upwind scheme is a more dissipative scheme compared to the others. Therefore, a TVD Superbee flux limiter is employed to avoid numerical oscillations at discontinuities and to minimize the numerical diffusion.

Furthermore, CLS shows excellent mass conservation for ellipsoidal and wobbling bubbles (see Fig. 9), where the mass conservation error is calculated by

$$M_r = [M(t) - M(0)]/M(0), \tag{24}$$

$$M(t) = \int_\Omega \phi dV, \tag{25}$$

and the tests were done with the finest grid using TVD Superbee flux limiter.

3.2. Wobbling bubbles

In this section, we present a numerical study of wobbling bubbles (See Fig. 10), where our results are compared with experimental correlations and numerical evidence (Terminal Reynolds,

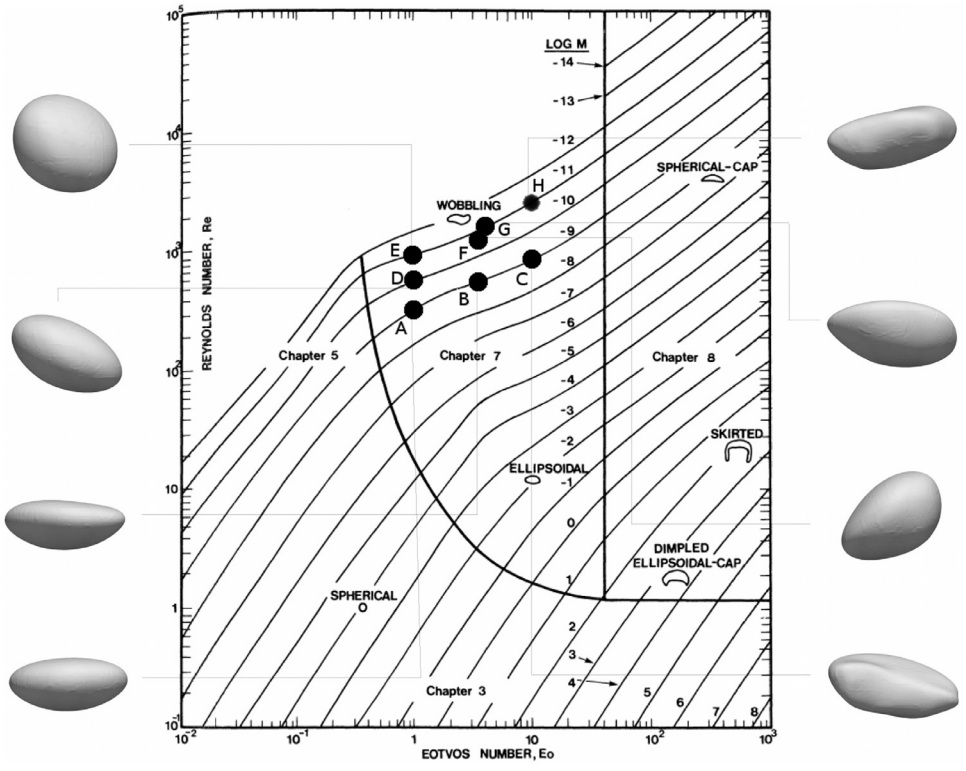

Fig. 10. Wobbling cases performed in this article pointed out in the Grace diagram by [20], and its respective bubble shape.

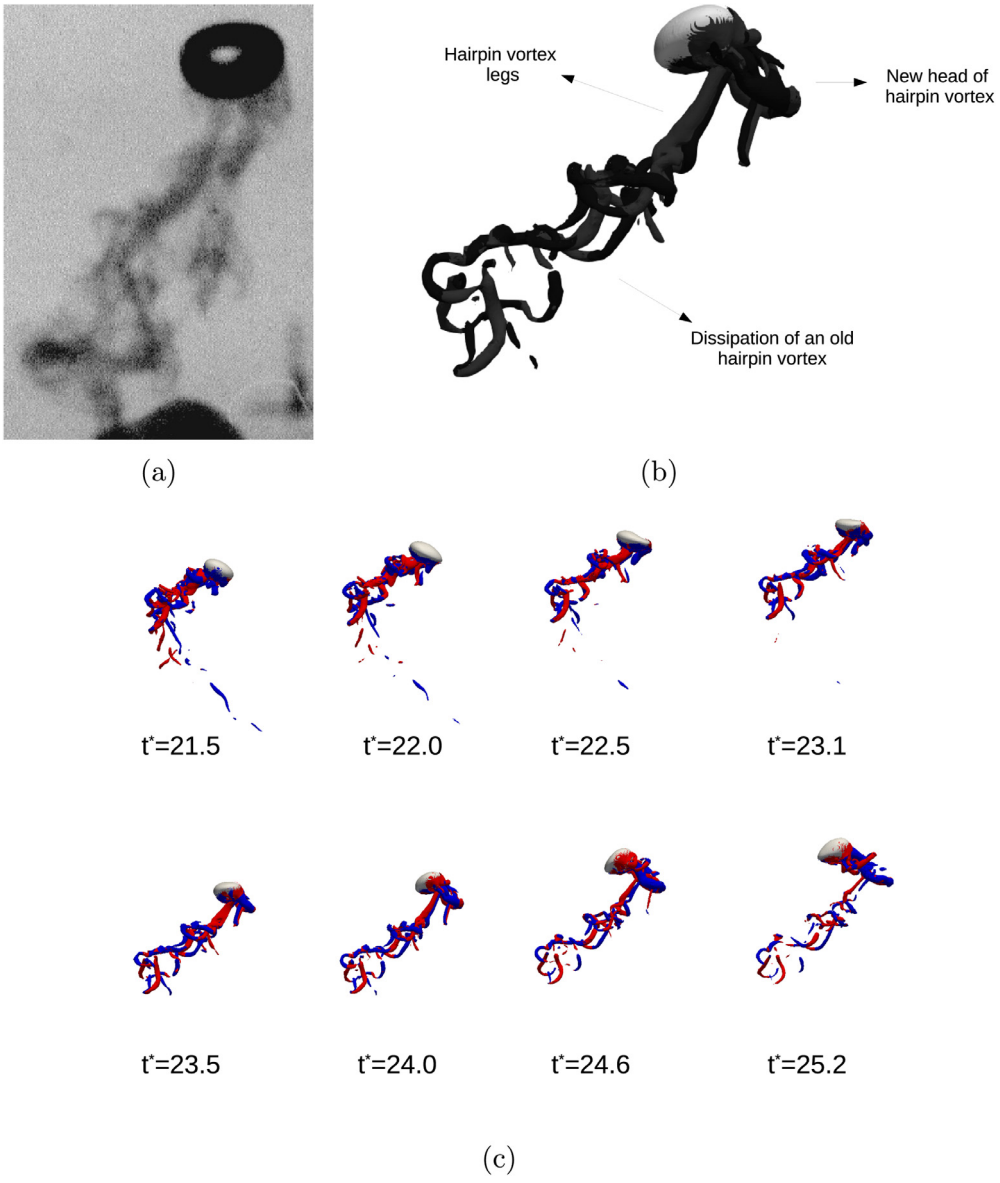

Fig. 11. Vortical structures presented in the wake of a wobbling bubble. (a) Visualization by [38] at Re ≈ 1500; (b) Highlight of hairpin vortex formation for the present simulation with Eo = 3.6, M = 2.5e−11; (c) Series of images showing the development and shedding of vortices for the case Eo = 3.6, M = 2.5e−11. (A video associated with this case can be found as suplemmentary material, in the online version, at doi:10.1016/j.compfluid.2019.04.013.)

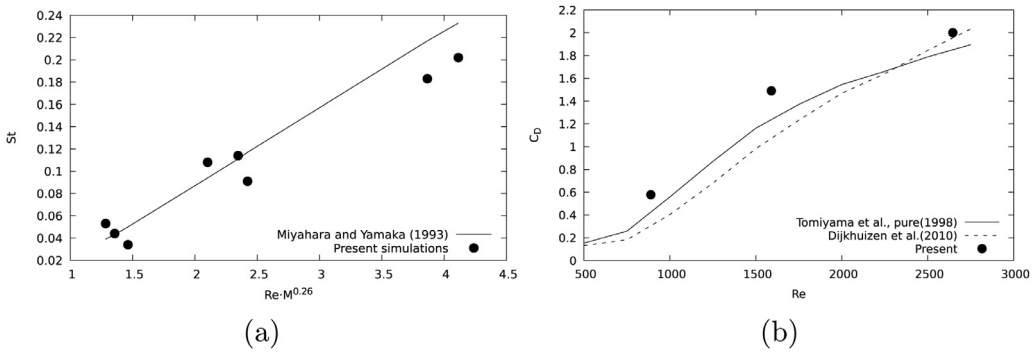

Fig. 12. (a) Present Strouhal number results compared with Miyahara and Yamaka correlation (see [43]); (b) Present drag coefficient results compared with [63] and [22] correlations for M = 1.0e−11.

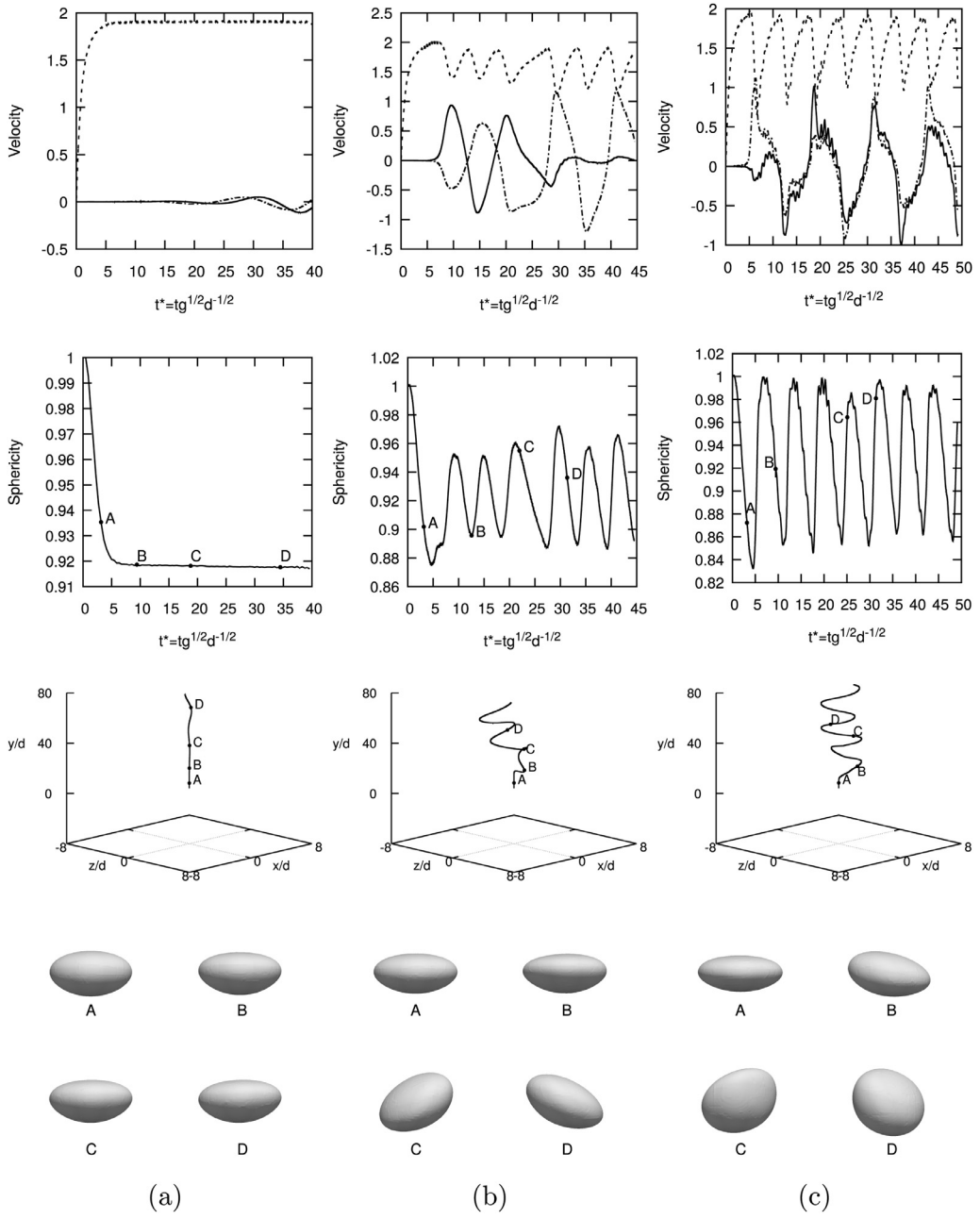

Fig. 13. Velocity components $[ug^{-1/2}d^{-1/2}(-\cdot-), vg^{-1/2}d^{-1/2}(--), wg^{-1/2}d^{-1/2}(-)]$, sphericity, 3D path and bubble shapes for (a) Eo = 1, M = 1e−9; (b) Eo = 1, M = 1e−10; (c) Eo = 1, M = 1e−11.

Strouhal number, Drag coefficient, and experimental image). Moreover, the effect of Eo and M are researched.

Dimensionless parameters used in these simulations are in Table 5.

The cases reported in this work start with a spherical bubble as the initial state. As it rises due to the buoyancy, it starts to transform into an oblate ellipsoidal with an unstable path. Moreover, AMR is used to get a resolution of 60 control volumes per diameter in the interface, and 30 control volumes for the near wake and the vortical structures. For most cases, the final mesh reaches around 1.8 M control volumes.

Table 5
Dimensionless numbers for the numerical cases in the wobbling regime.

Case	Eo	M	η_ρ	η_μ
A	1.0	1.0*e* − 09	100	100
B	3.6	1.0*e* − 09	100	100
C	10.0	1.0*e* − 09	100	100
D	1.0	1.0*e* − 10	100	100
E	1.0	1.0*e* − 11	100	100
F	3.6	2.5*e* − 11	100	54
G	4.0	1.0*e* − 11	100	100
H	10.0	1.0*e* − 11	100	100

3.2.1. Terminal Reynolds number and comparison with the experimental image

In Table 6, the average Reynolds number is reported and compared with experiments and numerical literature. The average velocity was calculated by discarding the initial overshoot (startup influences of the simulation) at $t^* = 0.3$. The comparison is made

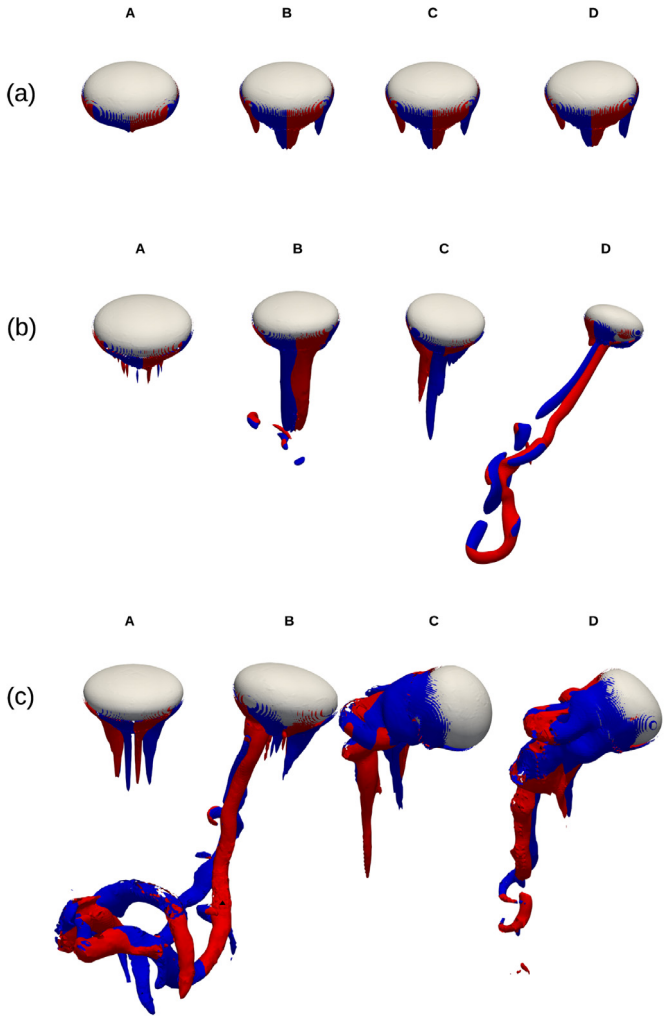

Fig. 14. Isosurfaces of the vorticity magnitude $||\omega||(d/g)^{1/2} = 8$, colored with vertical vorticity ω_y, where the red color corresponds to $\omega_y > 0$, the blue color corresponds to $\omega_y < 0$, and the letters A,B,C,D correspond to different dimensionless times as shown in Fig. 13 for (a) Eo = 1, M = 1e−9; (b) Eo = 1, M = 1e−10; (c) Eo = 1, M = 1e−11. (For interpretation of the references to colour in this figure legend, the reader is referred to the web version of this article.)

Table 6
Terminal Reynolds for the present simulations (Re_P) compared with the Grace diagram [32](Re_G), Tomiyama correlation [62](Re_T) and numerical simulations performed by [9]($Re_{Num.Ref}$).

Case	Eo	M	Re_G	Re_T	$Re_{Num.Ref}$	Re_P
A	1.0	1.0*e* − 09	320	280	320 − 350	340
B	3.6	1.0*e* − 09	530	480	–	467
C	10.0	1.0*e* − 09	900	830	730 − 740	797
D	1.0	1.0*e* − 10	540	500	–	514
E	1.0	1.0*e* − 11	930	880	710 − 970	856
F	3.6	2.5*e* − 11	1200	1200	–	1106
G	4.0	1.0*e* − 11	1700	1600	1600 − 1700	1512
H	10.0	1.0*e* − 11	2800	2600	2200 − 2300	2646

with the experimental correlations [32,62], and numerical results using different interface capturing methods [9]. Even with the complexity and chaotic behavior of wobbling bubbles, results are in close agreement with most of the numerical and experimental solutions reported in Table 6.

Experimental image of the vortical structures present on wobbling bubbles [38] are compared with the present simulation with Eo=3.6, M = 2.5e−11 (see Fig. 11). This case shows hairpin vortices, where the legs of these structures are attached to the lower side of the bubble. When a change of direction occurs on the path of the bubble, a new head of a counter-rotating hairpin vortex appears. In the meantime, the old hairpin vortices are shed downstream the wake (see Fig. 11c).

Table 7
Strouhal number for the present simulations (St_P) compared with Miyahara and Yamaka correlation (see [43])(St_{MY}), and numerical simulations performed by [41](St_M), [12](St_B), [29](St_G).

Case	Eo	M	St_{MY}	St_{Ref}	St_P
A	1.0	1.0*e* − 09	0.05	[0.09 − 0.108][b] St_M	0.034[a];0.09[b]
B	3.6	1.0*e* − 09	0.117	–	0.091[a]
C	10.0	1.0*e* − 09	0.233	–	0.202[a]
D	1.0	1.0*e* − 10	0.043	–	0.044[a]
E	1.0	1.0*e* − 11	0.039	–	0.053[a]
F	3.6	2.5*e* − 11	0.094	0.11[a] St_B; 0.093[a] St_G	0.108[a]
G	4.0	1.0*e* − 11	0.111	–	0.114[a]
H	10.0	1.0*e* − 11	0.217	–	0.183[a]

[a] $St = fd/U_T$ [12,13]
[b] $St = f\sqrt{2d/g}$ [41]

3.2.2. Strouhal number and drag coefficient

The accuracy of the methodology is assessed by the comparison of the Strouhal number and the drag coefficient with literature correlations. The Strouhal number has been defined by the following equation:

$$St = \frac{fd}{U_T}, \tag{26}$$

where f is the path oscillation frequency. Miyahara and Yamaka proposed a correlation (see [43]) to calculate St with path instabilities, in function of the Re and M.

$$St = 2.29 \times 10^{-2}\left(Re \cdot M^{0.26}\right)^{2.18-0.3821\ln\left(Re \cdot M^{0.26}\right)} \tag{27}$$

The Strouhal number obtained for the set of numerical cases are shown in Table 7 and Fig. 12a.

For the test cases, experimental and numerical results can be found in the literature by [12,29,41,43]. Our findings for the cases with similar conditions are in fair agreement with the literature correlation and numerical results. Moreover, it is also noticeable the increase of the Strouhal number as the Eo increase or the M decrease, due to the increase of bubble deformation and the evolution to more complex vortical structures leading to different oscillation paths.

The drag coefficient (C_D) has been calculated from the simulation using the following equation:

$$C_D = \frac{4(\rho_1 - \rho_2)gd}{3\rho_1 U_T^2} \tag{28}$$

Tomiyama et al. [63] presents a C_D model for non-spherical bubbles for a pure system in a simple form as:

$$C_D = max\left\{min\left[\frac{16}{Re}\left(1 + 0.15Re^{0.687}\right), \frac{48}{Re}\right], \frac{8}{3}\frac{Eo}{Eo+4}\right\} \tag{29}$$

Moreover, Dijkhuizen et al. [22] proposed a drag closure for both spherical and deformed bubbles, given by the next equation:

$$C_D = \sqrt{C_D(Re)^2 + C_D(Eo)^2} \tag{30}$$

with:

$$C_D(Re) = \frac{16}{Re}\left(1 + \frac{2}{1 + \frac{16}{Re} + \frac{3.315}{\sqrt{Re}}}\right) \tag{31}$$

$$C_D(Eo) = \frac{4Eo}{Eo + 9.5} \tag{32}$$

Please cite this article as: O. Antepara, N. Balcázar and J. Rigola et al., Numerical study of rising bubbles with path instability using conservative level-set and adaptive mesh refinement, Computers and Fluids, https://doi.org/10.1016/j.compfluid.2019.04.013

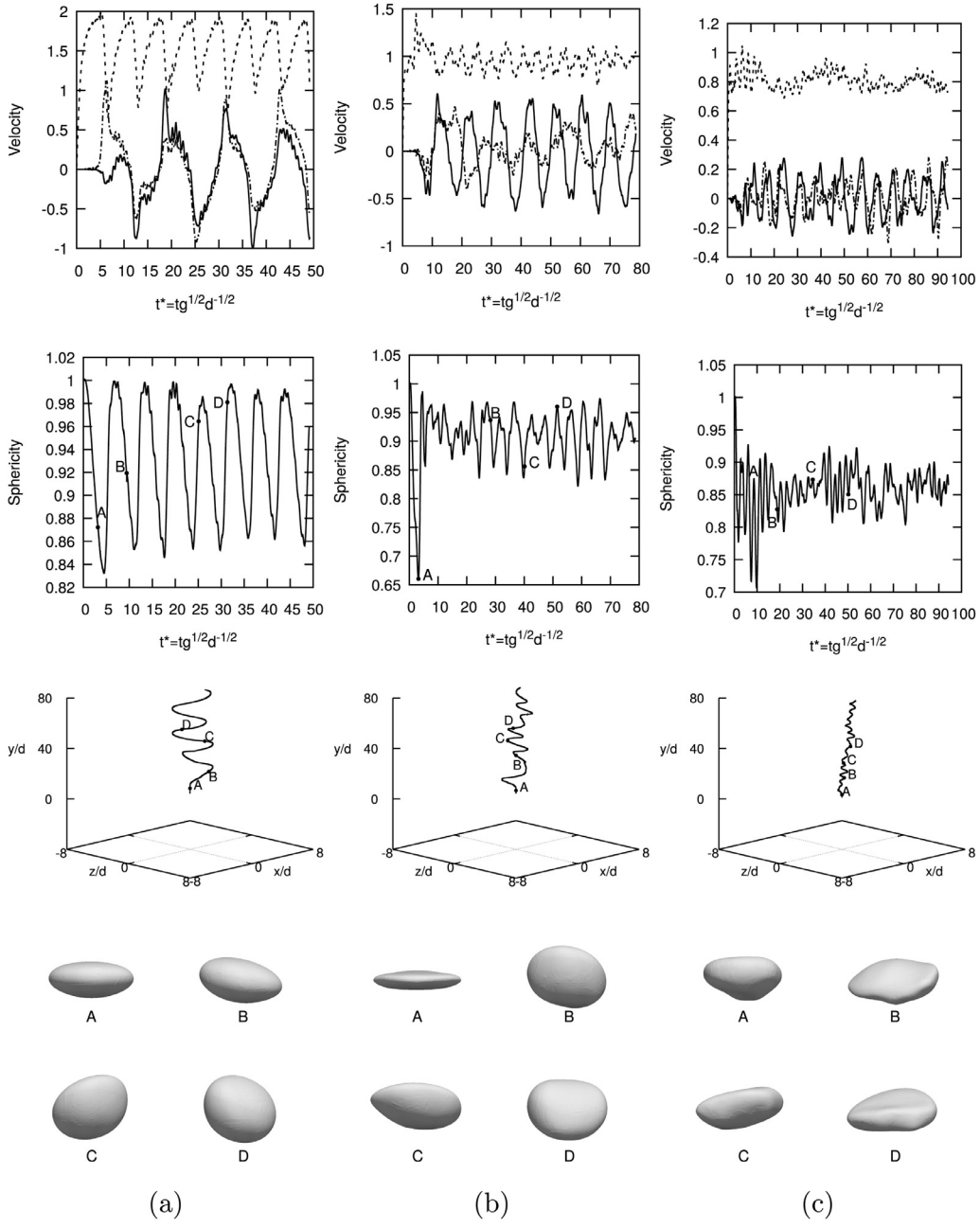

Fig. 15. Velocity components $[ug^{-1/2}d^{-1/2}(-\cdot-), vg^{-1/2}d^{-1/2}(--), wg^{-1/2}d^{-1/2}(-)]$, sphericity, 3D path and bubble shapes for (a) Eo = 1, M = 1e−11; (b) Eo = 4, M = 1e−11; (c) Eo = 10, M = 1e−11.

Table 8
Drag coefficient for the present simulations (C_{D_P}) compared with [63] correlation (see Eq. (29))(C_{D_T}), and [22] correlation (see Eq. (30))($C_{D_{Di}}$).

Case	Eo	M	C_{D_T}	$C_{D_{Di}}$	C_{D_P}
A	1.0	1.0*e* − 09	0.53	0.40	0.36
B	3.6	1.0*e* − 09	1.26	1.10	1.32
C	10.0	1.0*e* − 09	1.91	2.05	2.11
D	1.0	1.0*e* − 10	0.53	0.39	0.51
E	1.0	1.0*e* − 11	0.53	0.38	0.58
F	3.6	2.5*e* − 11	1.26	1.10	1.50
G	4.0	1.0*e* − 11	1.33	1.19	1.49
H	10.0	1.0*e* − 11	1.91	2.05	2.00

The C_D obtained for the set of numerical cases are shown in Table 8 and compared with the correlations of [22,63]. It can be noticed that as the Eo increase or M decrease, the drag coefficient increase, as a consequence of the bubble deformations and the increase of vorticity at the lower side of the bubble.

Finally, in Fig. 12b, the drag coefficient is plotted in function of the Reynolds number for M = 1.0e−11, and compared with the correlations.

These numerical results show that for low Eo, our findings are close to Tomiyama et al. [63] correlation and for higher Eo the results tend to Dijkhuizen et al. [22] correlation.

3.2.3. *Effect of Morton number* (M) *on the wobbling regime*

In this section, we show the main characteristics of the wobbling bubbles concerning M. The physical parameters, except for M, are fixed to Eo = 1.0, $\eta_\rho = \eta_\mu = 100$. The time variation of the velocity components, 3D path, and sphericity evolution are shown in Fig. 13.

Please cite this article as: O. Antepara, N. Balcázar and J. Rigola et al., Numerical study of rising bubbles with path instability using conservative level-set and adaptive mesh refinement, Computers and Fluids, https://doi.org/10.1016/j.compfluid.2019.04.013

In the case with $M = 1e{-}9$, the rising velocity and sphericity tend to a constant value, which is the result of a balance between buoyancy and viscous drag. Nevertheless, when the two horizontal velocity components start to oscillate, an unstable path is depicted (Fig. 13a). When M diminishes, a periodicity on the velocity components appears. Moreover, the amplitude of the oscillating velocity components and the frequency are increased. For the case with $M = 1e{-}10$, the horizontal velocity components are aligned between them, leading to a zigzag path (see Fig. 13b). It is also noticeable, the increase of bubble displacement in the horizontal direction as M decrease, mainly produced by the increase of the horizontal velocity components.

Sphericity is measured for these cases, where the decrease of M number makes the bubble to suffer frequently deformations. For the case with $M = 1e{-}9$, bubble shape remains mainly ellipsoidal, but with a decrease of M, the sphericity starts to oscillate. It is shown, the bubble reaches opposites states where it can be almost spherical or get a flat shape. These states are dictated by the oscillation of the inertial and surface tension forces, where high inertial forces produce a flat shape, and high surface tension forces show a spherical shape (see Fig. 13).

Isosurfaces of the vorticity magnitude are presented with fixed Eötvös number and different Morton number in Fig. 14. As the Morton number decreases, the hairpin vortices attached to the lower side of the bubble are getting more elongated, as a consequence of the increase of bubble deformations and vorticity generated at the base of the bubble. For the case with $M = 1e{-}9$, as seen in Fig. 14a, the vorticity generated in the wake is vertically aligned with the bubble, as a pair of counter-rotating vortices. Moreover, vorticity keeps a constant sign all along the trajectory. The numerical case with $M = 1e{-}10$ (see Fig. 14b) reveals vortex rings, which are simplified structures of the head loop of the hairpin vortex. Furthermore, for the case with $M = 1e{-}11$ the vorticity presents two longer counter-rotating threaded vortices which tend to wrap up around one another, dissipating the hairpin vortex head more efficiently (see Fig. 14c).

The case with Eo = 1.0 and $M = 1e{-}09$ is the limit where the bubble still presents no substantial shape deformations and small path oscillations, but as the Morton number decrease, bubble shape and velocity components frequently present oscillations. Bubble shape presents widely deformations going from flat to almost spherical, where this behavior is stronger as the Morton number gets smaller. Moreover, different vortical structures appear, such as axisymmetric two-thread vortex and long wrapped hairpin vortex. To sum up, as the vortex generation gets stronger, and the vortex structures are getting elongated, the horizontal bubble displacement increases as a mechanism of vortex shedding, which is quite noticeable when M decreases.

3.2.4. Effect of Eötvös number (Eo) on the wobbling regime

In this section, we show the main characteristics of the wobbling bubbles concerning Eo. The physical parameters, except for Eo, are fixed to $M = 1.0e{-}11$, $\eta_\rho = \eta_\mu = 100$. The time variation of the velocity components, 3D path, and sphericity evolution are shown in Fig. 15.

These cases have been selected with a small Morton number, where all of them present path instabilities. The bubble shape, velocities components, and path start to oscillate leading to a zigzag or spiraling movement. When Eo is increased, the amplitude of the velocity components decrease and its frequency increase. This behavior relates to the shrinking of the bubble displacement in the horizontal plane, generated by the bubble deformations and chaotic vortical structures.

Bubble shape measured by sphericity is shown in Fig. 15. As Eo decreases, the bubble shape oscillates with higher frequency and is less likely to reach a spherical shape during the oscillation, as it could get it at Eo = 1. In the case with highest Eötvös number, the bubble deformations are considerably noticeable and present local bulges (see Fig. 15c). These bulges are related to the chaotic creation of vortical structures appearing near the bubble.

In Fig. 16, illustrations of vortical structures are shown for each one of the studied cases. At small Eo, the main vortical structure is the hairpin vortex, where the legs are attached to the lower surface of the bubble, and in the meantime, the head of old hairpin vortices are being shed downstream (see Fig. 16a). As Eo increases, the bubble shape deforms frequently, the vorticity generation gets stronger, and the vortex structures are smaller (see Fig. 16b and c). For these cases, the bubble deformation plays an important role in the vortex shedding. Here, it is noticeable that vorticity generation increases, and the vortical structures changes from the elongated hairpin vortex, to small vortical structures. Moreover, the bubble presents a decrease in the horizontal displacement as the Eo increases (see Fig. 15). As a consequence of the vorticity generation at higher Reynolds, the bubble reduces its horizontal displacement, increase the bubble deformation by the presence of bulges and shortens the vortical structures as a mechanism of vortex shedding.

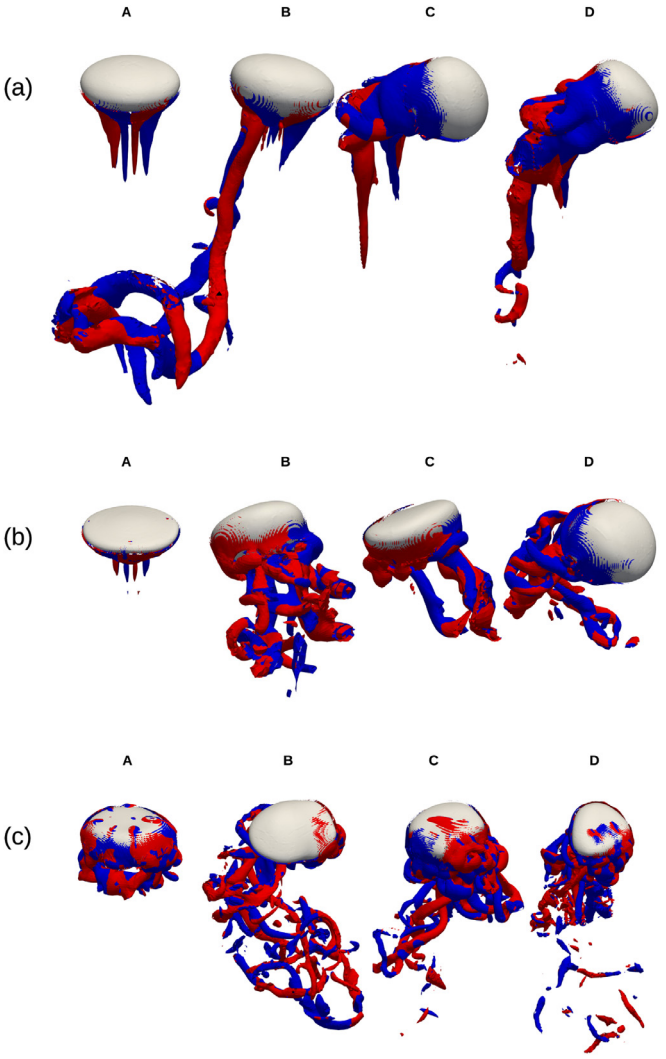

Fig. 16. Isosurfaces of the vorticity magnitude $||\omega||(d/g)^{1/2} = 8$, colored with vertical vorticity ω_y, where the red color corresponds to $\omega_y > 0$, the blue color corresponds to $\omega_y < 0$, and the letters A,B,C,D correspond to different dimensionless times as shown in Fig. 15 for (a) Eo = 1, $M = 1e{-}11$; (b) Eo = 4, $M = 1e{-}11$; (c) Eo = 10, $M = 1e{-}11$. (For interpretation of the references to colour in this figure legend, the reader is referred to the web version of this article.)

Please cite this article as: O. Antepara, N. Balcázar and J. Rigola et al., Numerical study of rising bubbles with path instability using conservative level-set and adaptive mesh refinement, Computers and Fluids, https://doi.org/10.1016/j.compfluid.2019.04.013

4. Conclusions

DNS of rising bubbles with path instability at high Reynolds number has been presented. The cases were selected at Morton number, $O(10^{-11})$ up to $O(10^{-9})$, and the Eötvös number was varied to observe the main differences in terminal velocities, bubble shape, vortical structures and oscillations paths.

The methodology consisted of a Conservative Level-Set method and Adaptive Mesh Refinement within a finite volume framework, which allowed to reproduce the main features of three-dimensional two-phase flows, combining an accurate representation of the interface, good mass conservation and a reduction of the computational effort. Moreover, the numerical methods have been verified and validated with previous empirical and numerical results from the literature, which include spurious currents in the static drop, and dynamic cases.

In the wobbling regime, terminal Reynolds number was compared with experimental and numerics references showing fair agreement for Reynolds number $\mathrm{Re} \sim O(10^2)$ and $\mathrm{Re} \sim O(10^3)$. The drag coefficient and the oscillation paths frequency were examined and compared to experimental correlation and some numerics. The results were appreciably good for most of the cases, where a vast domain is required to be able to capture the main global quantitative variables for all the cases.

The effect of the dimensionless numbers was reported. When $\mathrm{Eo} = 1$, and $1e{-}11 \leq M \leq 1e{-}09$, two filaments of counter-rotating vortex were found. Moreover, with the decrease of M those filaments are getting elongated, and hairpin vortex structures were observed. Under these conditions, the mechanism of vortex shedding was to increase the horizontal bubble displacement according to the vorticity generation.

For the cases, where $M = 1e{-}11$ and $1 \leq \mathrm{Eo} \leq 10$, vortex structures transformed from hairpin vortex to small vortical structures. At higher Eo the bubble shape presented bulges and large deformations. On these cases, as the Eo was increased, the vortex shedding leads to increase the bubble deformation with the presence of bulges, making the vortical structures smaller, and reducing the horizontal bubble displacement.

Acknowledgments

This work has been financially supported by the *MINECO*, Spain (ENE2017-88697-R), and by Termo Fluids S.L. Oscar Antepara acknowledges financial support in the form of a doctoral scholarship DI-14-06886 of the *MINECO* and 2015DI-68 of the *Generalitat de Catalunya*, Spain. Néstor Balcázar acknowledges the financial support of the *MINECO* (PTQ-14-07186), Spain. Three-dimensional simulations were carried out using computer time provided by PRACE 14th Call (Project 2016153612) and RES project(FI-2018-1-0025) through the MareNostrum IV supercomputer based in Barcelona, Spain. We acknowledge the Santander Supercomputacion support group who provided access to the Altamira Supercomputer (RES project FI-2018-3-0037).

Supplementary material

Supplementary material associated with this article can be found, in the online version, at doi:10.1016/j.compfluid.2019.04.013.

References

[1] Albert C, Kromer J, Robertson AM, Bothe D. Dynamic behaviour of buoyant high viscosity droplets rising in a quiescent liquid. J Fluid Mech 2015;778:485–533.
[2] Antepara O, Lehmkhul O, Borrell R, Chiva J, Oliva A. Parallel adaptive mesh refinement for large-eddy simulations of turbulent flows. Comput Fluids 2015;110:48–61.
[3] Balcázar N, Jofre L, Lehmkhul O, Castro J, Rigola J. A finite-volume/level-set method for simulating two-phase flows on unstructured grids. Int J Multiphase Flow 2014;64:55–72.
[4] Balcázar N, Lemhkuhl O, Rigola J, Oliva A. A multiple marker level-set method for simulation of deformable fluid particles. Int J Multiphase Flow 2015;74:125–42.
[5] Balcázar N, Lemhkuhl O, Jofre L, Oliva A. Level-set simulations of buoyancy-driven motion of single and multiple bubbles. Int J Heat Fluid Flow 2015;56:91–107.
[6] Balcázar N, Lemhkuhl O, Jofre L, Rigola J, Oliva A. A coupled volume-of-fluid/level-set method for simulation of two-phase flows on unstructured meshes. Comput Fluids 2016;124:12–29.
[7] Balcázar N, Rigola J, Castro J, Oliva A. A level-set model for thermocapillary motion of deformable fluid particles. Int J Heat Fluid Flow 2016;62(Part B):324–43.
[8] Balcázar N, Castro J, Rigola J, Oliva A. DNS Of the wall effect on the motion of bubble swarms. Procedia Comput Sci 2017;108C:2008–17.
[9] Baltussen MW, Kuipers JAM, Deen NG. A critical comparison of surface tension models for the volume of fluid method. Chem Eng Sci 2014;109:65–74.
[10] Bhaga D, Weber ME. Bubbles in viscous liquids: shapes, wakes and velocities. J Fluid Mech 1981;105:61–85.
[11] Brackbill JU, Kothe DB, Zemach C. A continuum method for modeling surface tension. J Comput Phys 1992;100:335–54.
[12] Brücker C. Structure and dynamics of the wake of bubbles and its relevance for bubble interaction. Phys Fluids 1999;11.
[13] Bothe D. VOF-Simulation of fluid particle dynamics. In: Sommerfeld M, editor. Proc. 11th Workshop on Two-phase Flow Predictions, Merseburg; 2005.
[14] Bothe D, Schmidtke M, Warnecke HJ. VOF-Simulation of the lift force for single bubbles in a simple shear flow. Chem Eng Technol 2006;29(9):1048–53.
[15] Chang YC, Hou TY, Merriman B, Osher S. A level-set formulation of eulerian interface capturing methods for incompressible two-phase flows. J Comput Phys 1996;124:462–88.
[16] Cano-Lozano JC, Martínez-Bazán C, Magnaudet J, Tchoufag J. Paths and wakes of deformable nearly spheroidal rising bubbles close to the transition to path instability. Phys Rev Fluids 2016;1:053604.
[17] Cano-Lozano JC, Bohorquez P, Martínez-Bazán C. Wake instability of a fixed axisymmetric bubble of realistic shape. Int J Multiphase Flow 2013;51:11–21.
[18] Ceniceros HD, Nos RL, Roma AM. Three-dimensional, fully adaptive simulations of phase-field fluid models. J Comput Phys 2010;229:6135–55.
[19] Chorin AJ. Numerical solution of the navier-stokes equations. Math Comput 1968;22:745–62.
[20] Clift R, Grace JR, Weber E. Bubbles, drops and particles. New York: Academic; 1978.
[21] De Vries AWG, Biesheuvel A, Van Wijngaarden L. Notes on the path and wake of a gas bubble rising in pure water. Int J Multiphase Flow 2002;28:1823–35.
[22] Dijkhuizen W, Roghair I, Van Sint Annaland M, Kuipers JAM. DNS Of gas bubbles behaviour using an improved 3d front tracking model-drag force on isolated bubbles and comparison with experiments. Chem Eng Sci 2010;65:1415–26.
[23] Duineveld PC. Rise velocity and shape of bubbles in pure water at high reynolds number. J Fluid Mech 1995;292:325–32.
[24] Ellingsen K, Risso F. On the rise of an ellipsoidal bubble in water: oscillatory paths and liquid-induced velocity. J Fluid Mech 2001;440:235–68.
[25] Ern P, Risso F, Fabre D, Magnaudet J. Wake-induced oscillatory paths of bodies freely rising or falling in fluids. Annu Rev Fluid Mech 2012;44:97–121.
[26] Esmaeeli A, Ervin E, Tryggvason G. Numerical simulations of rising bubbles. Bubble Dynamics and Interface Phenomena Fluid Mechanics and Its Applications, vol 23. Blake JR, Boulton-Stone JM, Thomas NH, editors; 1994.
[27] Giráldez H, Pérez Segarra CD, Oliet C, Oliva A. Heat and moisture insulation by means of air curtains: application to refrigerated chambers. Int J Refrig 2016;68:1–14.
[28] Favre F, Antepara O, Oliet C, Lehmkhul O, Pérez Segarra CD. An immersed boundary CFD method to conjugate heat transfer problems in complex geometries. application to an automotive antenna. Appl Therm Eng 2019;148:907–28.
[29] Gaudlitz D, Adams NA. Numerical investigation of rising bubble wake and shape variations. Phys Fluids 2008;21.
[30] Gaskell PH, Lau AKC. Curvature-compensated convective transport: SMART a new boundedness-preserving transport algorithm. Int J Numer Methods 1988;8:617–41.
[31] Gottlieb S, Shu CW. Total variation dimishing Runge-Kutta schemes. Math Comput 1998;67:73–85.
[32] Grace JR, Wairegi T, Nguyen TH. Shapes and velocities of single drops and bubbles moving freely through immiscible liquids. Trans Inst Chem Eng 1976;54:167–73.
[33] Gutiérrez E, Balcázar N, Bartrons E, Rigola J. Numerical study of taylor bubbles rising in a stagnant liquid using a level-set/moving-mesh method. Chem Eng Sci 2017;164:158–77.
[34] Hirt C, Nichols B. Volume of fluid (VOF) method for the dynamics of free boundary. J Comput Phys 1981;39:201–25.
[35] Hua JS, Lin P, Stene JF. Numerical simulation of gas bubbles rising in viscous liquids at high reynolds number. In: Moving Interface Problems and Applications in Fluid Dynamics, Contemporary Mathematics, 466, American Math Society; 2008. p. 17–34.
[36] Hysing S. Mixed element FEM level set method for numerical simulation of immiscible fluids. J Comput Phys 2012;231:2449–65.

Please cite this article as: O. Antepara, N. Balcázar and J. Rigola et al., Numerical study of rising bubbles with path instability using conservative level-set and adaptive mesh refinement, Computers and Fluids, https://doi.org/10.1016/j.compfluid.2019.04.013

[37] Koebe M, Bothe D, Warnecke HJ. Direct numerical simulation of air bubbles in water/glycerol mixtures: shapes and velocity fields. In: In ASME/JSME 2003 4th Joint Fluids Summer Engineering Conference, 2; 2003. p. 415–21. Paper No. FEDSM2003–45154
[38] Lunde K, Perkins RJ. Observations on wakes behind spheroidal bubbles and particles. Vancouver, Canada: ASMEFED Summer Meeting; 1995. Paper No. FEDSM 97–3530
[39] Magnaudet J, Eames I. The motion of high-reynolds-number bubbles in inhomogeneous flows. Annu Rev Fluid Mech 2000;32(1):659–708.
[40] Magnaudet J, Mougin G. Wake instability of a fixed spheroidal bubble. J Fluid Mech 2007;572:311–37.
[41] Mougin G, Magnaudet J. Path instability of a rising bubble. Phys Rev Lett 2002;88(1).
[42] Mougin G, Magnaudet J. Wake-induced forces and torques on a zigzagging/spiralling bubble. J Fluid Mech 2006;567:185.
[43] Miyahara T, Yamaka S. Mechanics of motion and deformation of a single bubble rising through quiescent highly viscous newtonian and non-newtonian media. J Chem Eng 1993;26(3):297–302.
[44] Olsson E, Kreiss G. A conservative level set method for two phase flow. J Comput Phys 2005;210:225–46.
[45] Osher S, Sethian JA. Fronts propagating with curvature-dependent speed: algorithms based on hamilton-jacobi formulations. J Comput Phys 1988;79:175–210.
[46] Peskin CS. Numerical analysis of blood flow in the heart. J Comput Phys 1977;25:220–52.
[47] Pivello MR, Villar MM, Serfaty R, Roma AM, Silveira-Neto A. A fully adaptive front tracking method for the simulation of two phase flows. Int J Multiphase Flow 2014;58:72–82.
[48] Popinet S. Gerris a tree-based adaptive solver for the incompressible euler equations in complex geometries. J Comput Phys 2003;190:572–600.
[49] Prosperetti A. Bubbles. Phys Fluids 2004;16(6):1852–65.
[50] Prosperetti A, Ohl C, Tijink A, Mougin G, Magnaudet J. Leonardos paradox. appendix to a. prosperetti, c. d. ohl, a. tijink. J Fluid Mech 2003;482:286–9.
[51] Rhie CM, Chow WL. Numerical study of the turbulent flow past an airfoil with trailing edge separation. AIAA J 1983;21:1525–32.
[52] Saffman PG. On the rise of small air bubbles in water. J Fluid Mech 1956;1:249–75.
[53] Schillaci E, Jofre L, Balcázar N, Antepara O, Oliva A. A low-dissipation convection scheme for the stable discretization of turbulent interfacial flow. Comput Fluids 2017;153:102–17.
[54] Schillaci E, Antepara O, Balcázar N, Rigola J, Oliva A. A numerical study of liquid atomization regimes by means of conservative level-set simulations. Comput Fluids 2019;179:137–49.
[55] Sharaf DM, Premlata AR, Tripathi MK, Karri B, Sahu KC. Shapes and paths of an air bubble rising in quiescent liquids. Phys Fluids 2017;29:122104.
[56] Smolianski A, Haario H, Luukka P. Vortex shedding behind a rising bubble and two-bubble coalescence: a numerical approach. Appl Math Model 2005;29(7):615–32.
[57] Sussman M, Smereka P, Osher S. A level set approach for computing solutions to incompressible two-phase flow. J Comput Phys 1994;144:146–59.
[58] Sussman M, Almgren AS, Bell JB, Colella P, Howell LH, Welcome ML. An adaptive level set approach for incompressible two-phase flows. J Comput Phys 1999;148:81–124.
[59] Sweby PK. High resolution using flux limiters for hyperbolic conservation laws. SIAM J Numer Anal 1984;21:995–1011.
[60] Tchoufag J, Magnaudet J, Fabre D. Linear stability and sensitivity of the flow past a fixed oblate spheroidal bubble. Phys Fluids 2013;25(5):054108.
[61] Termo Fluids S.L. Webpage: www.termofluids.com.
[62] Tomiyama A. Struggle with computational bubble dynamics. In: Third International Conference on Multiphase Flow; 1998. p. 369–405.
[63] Tomiyama A, Kataoka I, Zun I, Sakaguchi T. Drag coefficients of single bubbles under normal and micro gravity conditions. JSME Int J Ser B 1998;41(2).
[64] Torras S, Oliet C, Rigola J, Oliva A. Drain water heat recovery storage-type unit for residential housing. Appl Therm Eng 2016;103:670–83.
[65] Tripathi MK, Sahu KC, Govindarajan R. Dynamics of an initially spherical bubble rising in quiescent liquid. Nat Commun 2015;6.
[66] Tryggvason G, Bunner B, Esmaeeli A, Juric D, Al-Rawahi N, Tauber W, Han J, Nas S, Jan Y-J. A front-tracking method for the computations of multiphase flow. J Comput Phys 2001;169:708–59.
[67] Unverdi S, Tryggvason G. A front-tracking method for viscous, incompressible, multifluid flows. J Comput Phys 1992;100:25–37.
[68] Van Sint Annaland M, Deen NG, Kuipers JAM. Numerical simulation of gas bubbles behaviour using a three-dimensional volume-of-fluid method. Chem Eng Sci 2005;60:2999–3011.
[69] Veldhuis CHJ, Biesheuvel A, Van Wijngaarden L. Shape oscillations on bubbles rising in clean and in tap water. Phys Fluids 2008;20(4):040705.

Please cite this article as: O. Antepara, N. Balcázar and J. Rigola et al., Numerical study of rising bubbles with path instability using conservative level-set and adaptive mesh refinement, Computers and Fluids, https://doi.org/10.1016/j.compfluid.2019.04.013